

Inner-shell photoionization of atomic chlorine

W. C. Stolte,^{1,2} Z. Felfli,³ R. Guillemin,⁴ G. Öhrwall,⁵ S.-W. Yu,⁶ J. A. Young,¹ D. W. Lindle,¹ T. W. Gorczyca,⁷
N. C. Deb,^{8,*} S. T. Manson,⁹ A. Hibbert,⁸ and A. Z. Msezane³

¹Department of Chemistry, University of Nevada, Las Vegas, Nevada 89154-4003, USA

²Advanced Light Source, Lawrence Berkeley National Laboratory, Berkeley, California 94720, USA

³Center for Theoretical Studies of Physical Systems, Clark Atlanta University, Atlanta, Georgia 30314, USA

⁴LCPMR, UPMC, and CNRS (UMR7614), 11 rue Pierre et Marie Curie, 75231 Paris Cedex 05, France

⁵MAX-Lab, Lund University, P. O. Box 118, 22100, Lund, Sweden

⁶Lawrence Livermore National Laboratory, Livermore, California 94550, USA

⁷Department of Physics, Western Michigan University, Kalamazoo, Michigan 49008, USA

⁸Centre for Theoretical Atomic, Molecular and Optical Physics, Queen's University Belfast, Belfast BT7 1NN,
Northern Ireland, United Kingdom

⁹Department of Physics and Astronomy, Georgia State University, Atlanta, Georgia 30303, USA

(Received 13 June 2013; published 25 November 2013)

Relative partial cross sections have been measured following photoexcitation of atomic chlorine near the Cl $2p$ and Cl $1s$ ionization thresholds. In addition, Breit-Pauli R -matrix calculations have been carried out in the region of the $2p$ thresholds, and the results are compared with experiment. Owing to angular-momentum considerations, it was found that the resonances associated with the higher $2p^{-1}$ thresholds should be significantly wider than the lower ones, and this is borne out in both the experimental and the theoretical results. It is shown that a large number of resonance series contribute to the cross section, which make it difficult to untangle, and suggestions for further work to better understand the spectra are presented.

DOI: [10.1103/PhysRevA.88.053425](https://doi.org/10.1103/PhysRevA.88.053425)

PACS number(s): 32.80.Fb, 32.80.Hd

I. INTRODUCTION

The study of inner-shell photoionization of open-shell atoms poses a number of challenges. From an experimental point of view, the difficulties involve sample preparation: creating a large enough density of free atoms to perform a measurement, together with a large enough photon flux [1–10]. On the theoretical side, in dealing with the removal of inner-shell electrons, one must include the processes that fill the resulting vacancy, radiative decay along with participator and spectator Auger decay, to have any hope of quantitative accuracy [11–15]. In addition, the open-shell character leads to multiplet structures which in turn translate to multiple inner-shell thresholds and channels; and there can be radiationless Coster-Kronig-like transitions among these multiplet channels. For the above reasons, most of the extant atomic photoionization work has been done on closed-shell systems, and mostly for outer shells. Nevertheless, the Periodic Table is comprised largely of open-shell atoms, and, aside from the interest in their photoionization from a basic physics point of view, such data are also of applied importance in a number of connections, e.g., astrophysics and aeronomy [16–18]. Note, however, that there does exist a number of studies of open-shell atoms; see, e.g., Ref. [19].

One of the most studied atoms is Ar, concerning photoionization from both outer and inner shells [20–26]. Thus, looking at an adjacent atom in the Periodic Table would allow us to study a similar system and spotlight the differences in the photoionization engendered by the existence of an open outer shell. The Cl atom is an appropriate candidate, with outer shell structure $3p^5$ as compared to the $3p^6$ outer shell of Ar. Thus,

we have undertaken a combined high-resolution experimental and theoretical investigation of inner-shell photoabsorption of atomic Cl. Note that some lower-resolution experimental results for photoionization in the vicinity of the $2p$ thresholds have been reported [4,7,9], but none, as far as we know, in the vicinity of the opening of the K shell. Furthermore, there is only a single theoretical study reported of inner-shell photoionization of Cl beyond the central-field model (which cannot be realistic near thresholds because multiplet structure and resonances are omitted), and this is a semiempirical but extensive calculation based on the Fano configuration-interaction methodology [13].

In this paper we report on high-resolution measurements of the photoionization of atomic chlorine in the vicinity of the $L_{2,3}$ ionization thresholds, along with relativistic Breit-Pauli R -matrix calculations. In addition, measurements in the vicinity of the K -shell thresholds also are reported. The experimental techniques are described in Sec. II, the data reduction is described in Sec. III, and the theoretical methodology is discussed in Sec. IV. Section V presents and discusses the results and compares experiment with theory. The final section presents a summary and conclusions.

II. EXPERIMENTAL TECHNIQUE

The experimental technique is similar to that previously described for our measurements on atomic nitrogen [10] and atomic oxygen [27], and those of Samson *et al.* [1,28]. The measurements were performed on undulator beamline 8.0.1.3 and bending magnet beamline 9.3.1 at the Advanced Light Source (Lawrence Berkeley National Laboratory, Berkeley, CA, U.S.A.).

Calibration of the photon energy at the $2p$ edge was done by comparison with results of Shaw *et al.* [29,30] using the Cl $(2p_{3/2})^{-1}4s$ molecular chlorine transition at 204.240 eV.

*Present address: Indian Maritime University, Kolkata Campus, P-19 Taratala Road, Kolkata-700 088, India.

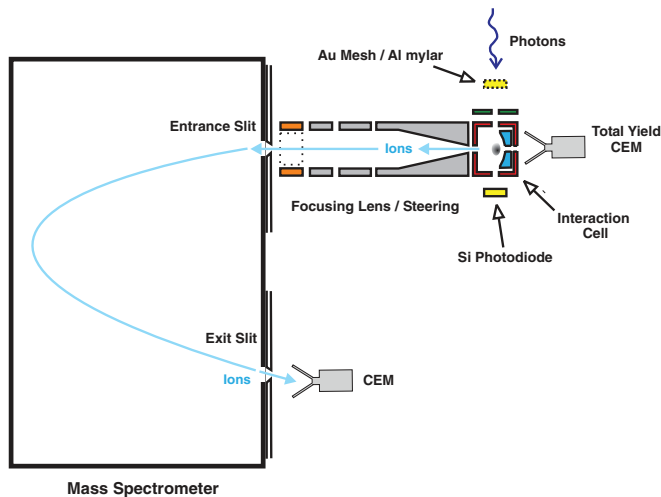


FIG. 1. (Color online) Schematic diagram of the apparatus showing the interaction region, all of the focusing and steering elements, and the entrance and exit slits of the magnetic mass spectrometer, I_0 mesh or foil, silicon diode, the total-yield detector, and the partial-ion-yield detector (see Fig. 2 for the gas flow tubes).

We observed a photon energy shift of 42 meV between our molecular chlorine calibration procedure and the published results of Caldwell *et al.* [7] and those of Martins [13]. We estimated a monochromator resolution of 30 meV near 205 eV photon energy by comparing the well-separated $4s(^3D)^2D_{5/2}$ atomic chlorine transition at 204.76 eV with the theoretical lifetime of 5.3 meV [13]. Calibration at the Cl $1s$ edge was performed by comparison to results of Perera *et al.* [31] using the Cl $(1s)^{-1}11a_1$ transition in CF_3Cl at 2823.5 eV. We estimated the incident radiation near the Cl K edge to have a resolution of 0.5 eV by measuring the Cl $(1s)^{-1}6\sigma^*$ transition in HCl in comparison to our previous results [32].

As described previously, the experimental apparatus consisted of a mass spectrometer, an ion source with suitable lensing, and a detector [33]. The transit time for ions to pass through the mass spectrometer is a few microseconds. Figure 1 gives a brief overview of the instrument's current configuration. Photons from the beamline pass through a gold mesh or 0.8- μm -thick aluminum foil and provide the incident flux measurement I_0 . The photons enter the gas cell through an entrance collimator which minimizes the possibility of having scattered electrons enter the interaction region. The gas cell has a curved extraction plate which increases the solid angle of acceptance by focusing the ions into the lens system. The Einzel lens system and steering plates focus and direct the ions onto the mass spectrometer entrance slit. Ions are detected at the exit slit of the spectrometer with a Dr. Sjutts channel electron multiplier (type KBL-15RS-EDR). An analog signal from a capacitance manometer was recorded simultaneously with the ion signal to monitor target gas pressure. Finally, the photon intensity was monitored after the gas cell with a Si photodiode, I . The flux measurements were constantly compared (I_0/I) to ensure there was no observed spectral structure caused by contamination of either measurement.

Atomic Cl was produced in a microwave discharge system by the dissociation of molecular chlorine (see Fig. 2). The

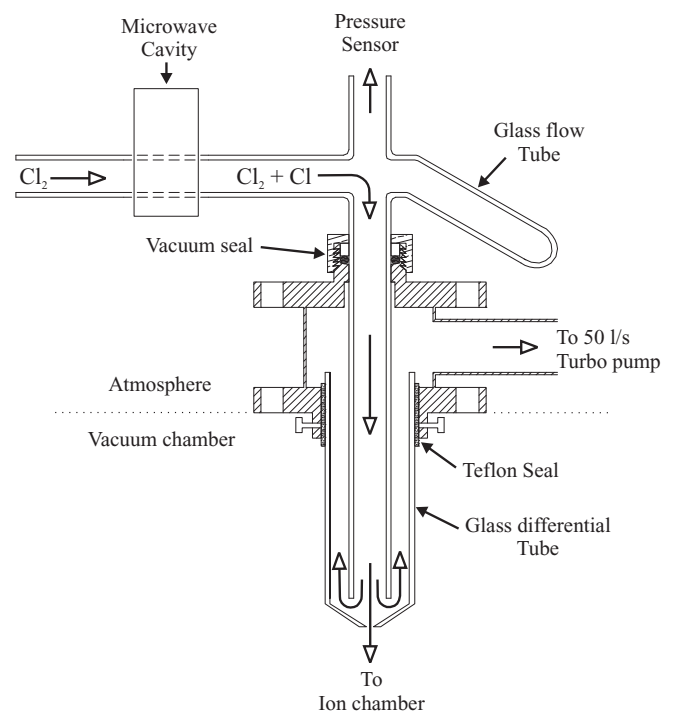


FIG. 2. Diagram of the gas flow tubes and microwave cavity used for the production of atomic chlorine (see text for details).

target was commercially obtained as a 99.996% pure liquified gas from Scott Specialty Gases, and was used without further purification. Approximately 5% molecular dissociation was produced when the L-shaped Pyrex flow tube surrounded by the microwave cavity was coated with Teflon. It was further increased to about 15% when this tube was additionally coated with phosphorus pentoxide, and subsequently exposed to atmospheric humidity before installing it in the vacuum system. The remaining Pyrex tubing was coated on the inside with Teflon. It was found that collisions with the walls of these coated tubes strongly quenched the chlorine atoms created in long-lived metastable states, and also reduced wall recombination effects, before the ions reached the interaction region, leaving only ground-state atoms and molecular chlorine to interact with the x rays [1]. Additionally, the Pyrex differential tube was carbon coated on the outside, to keep the glass surface from electrically charging and subsequently causing stray electric fields inside the gas cell. The discharge products were constrained to flow past a small orifice of 0.5 mm diameter before entering the gas cell. An additional convectron vacuum pressure gauge was attached to the flow tubes to monitor the gas pressure (~ 250 mTorr) during the duration of the experimental period. The gas flow rate through the Pyrex tubing was increased by pumping on the flow tubes with a 50 l/s Leybold turbopump, thus maintaining a fast flow through the glass flow tube to further reduce wall recombination effects. We also satisfied the electron-cyclotron resonance condition by superimposing on the microwave cavity a constant magnetic field perpendicular to the 2.45 GHz electric field. The magnetic field aided in confinement and electron-cyclotron heating of the plasma. Coupled with the faster gas flow rate, this increased the dissociation fraction to near 30%.

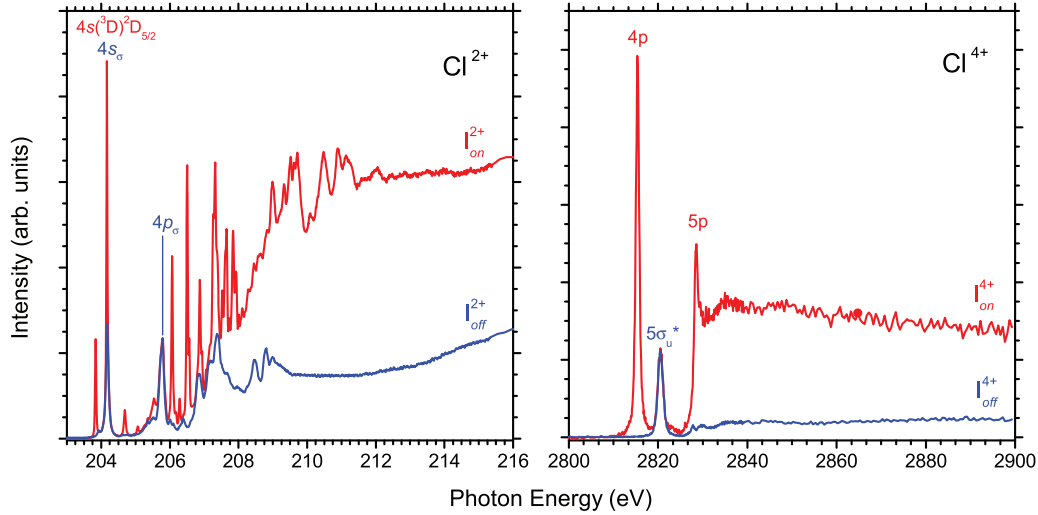


FIG. 3. (Color online) A spectral comparison of microwave-on state, a mixture of atomic Cl and Cl₂ (red), and microwave-off state, pure Cl₂ (blue), to visually demonstrate the subtraction procedure.

III. DATA REDUCTION

The partial-ion yields measured with the discharge *on* as described above include contributions from both ground-state atomic chlorine and molecular Cl₂, differing as a function of photon energy, whereas, with the discharge *off* the gas target is composed of molecular Cl₂ only. Because the spectroscopy of molecular Cl₂ is known [30], its presence provides an internal energy calibration. The cross section $\sigma^{q+}(E)$, as a function of photon energy E for photoionization of atomic chlorine to an ion of charge $+q$ can be obtained from [28]

$$\sigma^{q+}(E) = C_{q+}(I_{\text{on}}^{q+} - f \times I_{\text{off}}^{q+}), \quad (1)$$

where I_{on}^{q+} and I_{off}^{q+} are normalized ion yields measured as functions of photon energy with the microwave discharge on or off, and C_{q+} is a constant dependent on the number density of chlorine atoms and the ion-collection efficiency of the apparatus. Figure 3 shows two comparative samples of these spectra, one for Cl²⁺ at the L edge and the other for Cl⁴⁺ at the K edge. Relative data for single and multiple photoionization of Cl₂ [30] were used to determine values for the constants C_{q+} . The parameter $f = n(\text{Cl}_2^{\text{on}})/n(\text{Cl}_2^{\text{off}})$, with $n(\text{Cl}_2^{\text{on}})$ and $n(\text{Cl}_2^{\text{off}})$ being number densities of Cl₂ with the microwave discharge on or off, represents the fraction of Cl₂ molecules that do not dissociate in the discharge. The value of f is empirically chosen for each fragment ion to eliminate the molecular peaks from the measured ion yields via a weighted subtraction [2,28]. Fortunately there is a molecular chlorine resonance at 205.79 eV, $(2p_{3/2})^{-1}4p_{\sigma}$, which does not overlap significantly with any of the atomic transitions, while the $(1s)^{-1}5\sigma_u^*$ resonance at 2820.6 eV plays this role at the K edge. As noted above, the total dissociation fraction $1 - f$ was about 30%. Finally, the collection efficiency for each ion Cl^{q+} produced by photoionization of atomic chlorine was assumed equal to the collection efficiency of the same ion generated in dissociative photoionization of Cl₂.

This procedure works extremely well at the L edge for the Cl²⁺ and Cl³⁺ fragments, but it does not work well for Cl⁺ because the cross section for creating Cl⁺ from Cl₂ is

significantly larger than its creation from atomic Cl, and the discharge-on spectra have slightly wider linewidths for the lower-charged fragment ions. Likewise, Cl³⁺, Cl⁴⁺, Cl⁵⁺, and Cl⁶⁺ gave better results at the K edge.

The resulting spectra were fitted with WINXAS [34] and its near-edge x-ray-absorption fitting routines. The spectral lines were fitted with Voigt functions, with the Gaussian contribution to each peak held at a constant width equal to the measured monochromator resolution, while the Lorentzian portion of the function, which represents the lifetime of the particular state, was allowed to vary. Arctan functions were used to represent the ionization thresholds, with their slopes set to the beamline resolution and their positions allowed to vary after initially setting them using literature values [13]. The fitted peak energies and lifetimes for the L edge are given in Table I. The $3p$ and $4p$ transitions following K -edge excitation are located at 2815.4(1) and 2828.6(1), and the ionization threshold is estimated to be at 2829.2(5) eV. All errors include standard deviations and calibration errors.

IV. THEORY

Photoionization of Cl in the vicinity of the $2p^{-1}$ inner-shell thresholds is investigated within the framework of the R -matrix method [35]. There, the wave function is represented by an expansion which can be formally written as

$$\Psi_k = \mathcal{A} \sum_i \Phi_i(R) \sum_j c_{ijk} u_{ij}(r) + \sum_{\alpha} d_{\alpha k} \chi_{\alpha}(R, r). \quad (2)$$

Here R stands for the collective coordinates of the target ion electrons, Φ_i are wave functions for the various states of Cl⁺, known as target ionic states in R -matrix terminology (the outer electron's spin and angular momenta are implicitly coupled to this wave function), the $u_{ij}(r)$ are basis functions for the outer ("continuum" or "Rydberg") electron's orbital, \mathcal{A} is the antisymmetrization operator, and the coefficients c_{ijk} and $d_{\alpha k}$ are determined from variational considerations. The N -electron target wave functions Φ_i are linear combinations of configurations ϕ_k [a configuration-interaction (CI) expansion]

TABLE I. Experimental energies of major transitions of atomic Cl following Cl $2p$ excitation, along with their tentative identifications. All errors in the table are standard deviations; total errors must include a calibration error of 20 meV from our use of the molecular chlorine $(2p_{3/2})^{-1}4s_{\sigma}$ transition [29,30]. When possible comparison is made to [7]. N corresponds to an index number used to identify the experimental transitions observed in Fig. 4.

N	Configuration	Present experiment		Previous experiment [7]	
		Energy (eV)	Γ (meV)	Energy (eV)	Γ (meV)
1	$4s(^1P)^2P_{1/2,3/2}$	203.913(2)	16	203.949	22
2	$4s(^3D)^2D_{5/2}$	204.238(1)	8.5	204.268	16
3	$4s(^3D)^4D_{5/2}$	204.766(2)	43	204.787	
4		205.138(4)	59		
5	$4s(^3P)^2P_{3/2}$	205.618(2)	156		
6	$3d(^1P)^2D_{5/2}$	206.144(2)	25	206.147	22
10	$3d(^2D)^2D_{5/2}, ^2S_{1/2}, ^2P_{3/2}$	206.581(2)	35	206.576	40
11	$5s(^3D)^2D_{5/2}$	206.647(3)	47	206.640	
13	$4d(^1P)^2P_{3/2}$	206.944(5)	27	206.933	
15	$4d(^3D)^2D_{5/2}$	207.333(10)	34	207.328	
16	$4d(^3D)^2P_{1/2}, 6s(^3D)^2D_{5/2},$ $3d(^3D)^4D_{1/2}$	207.390(10)	40	207.376	
17	$4s(^1D)^2D_{5/2}, 3d(^3D)^2S_{1/2}$	207.448(20)	40	207.438	
18		207.563(15)	32		
20	$5d(^3D)^2D_{5/2}, ^2S_{1/2}, ^2P_{3/2}$	207.732(15)	12	207.705	
22	$7d(^3D)^2D_{5/2}, 6s(^3D)^4D_{1/2},$ $4d(^3D)^2P_{3/2}, 7d(^3D)^4P_{1/2},$ $8d(^3D)^2D_{5/2}$	207.806(15)	25	207.880	
23	$3d(^3P)^2P_{1/2}, 3d(^3D)^2P_{3/2},$ $9d(^3D)^2D_{5/2}, ^2P_{3/2}, 10d(^3D)^2D_{5/2}$	207.911(10)	71	207.975	

formed by coupled Slater determinants of atomic orbitals:

$$\Phi_i(R) = \sum_m U_{im} \phi_m(R) \quad \text{or} \quad \Phi = \mathbf{U}\phi. \quad (3)$$

The coefficients U_{im} form a unitary matrix that diagonalizes the ionic Hamiltonian within the basis Φ_i :

$$\langle \Phi_{i'} | \mathcal{H}(\text{Cl}^+) | \Phi_i \rangle = E_i \delta_{i'i'} \quad \text{or} \quad \mathbf{U}^\dagger \mathbf{H} \mathbf{U} = \mathbf{E}, \quad (4)$$

where $\mathbf{H}_{mm'} = \langle \phi_m | \mathcal{H}(\text{Cl}^+) | \phi_{m'} \rangle$ and \mathbf{E} is a diagonal matrix of ionic eigenenergies. The χ_{α} are additional $(N+1)$ -electron configurations constructed from only the target atomic orbitals, so they are completely contained within the R -matrix ‘‘box.’’ Their inclusion is necessary to compensate for the restriction that the $u_{ij}(r)$ are orthonormal to all target orbitals making up the target states, thereby making the set of basis orbitals more complete. In order to account for the broadening, due to spectator Auger decay, of the $2p^5 3s^2 3p^5 ns, md$ inner-shell photoexcited resonances, an optical potential is introduced. This approach was shown to give excellent agreement with experimental inner-shell photoionization spectra in Ar [36], Ne [37], and O [38]. Fine-structure splitting of the various levels is incorporated via the Breit-Pauli operator.

In the construction of the CI target wave functions of Cl^+ , the radial orbitals $1s, 2s, 2p, 3s, 3p, 3d, 4s, 4p, 4d, 4f, 5s, 5p,$ and $5d$ were used, with the $1s$ and $2s$ being those of the ground state of Cl^+ given by Clementi and Roetti [39]. The orbitals $2p, 3s,$ and $3p$ were optimized on the energy of the $1s^2 2s^2 2p^5 3s^2 3p^5$ ($^1P^e$) LS state. This was done in order to bring the energies of $2p$ -hole states closer to the experimental energies. The orbitals $3d, 4s, 4p, 4d, 4f, 5s, 5p,$ and $5d$

were optimized on the energies of the $3s^2 3p^3(^4S^o) 3d^5 D^o,$ $3s^2 3p^3(^4S^o) 4s^5 D^o,$ $3s^2 3p^3(^4S^o) 4p^5 P^o,$ $3s^2 3p^3(^4S^o) 3d^3 D^o,$ $3s^2 3p^3(^2D^o) 4p^3 F^o,$ $3s^2 3p^3(^4S^o) 4s^5 S^o,$ $3s^2 3p^3(^4S^o) 4p^5 P^o,$ and $3s^2 3p^3(^4S^o) 3d^3 D^o,$ respectively, using the program CIV3 [40]. The orbitals $3d, 4s,$ and $4p$ are, therefore, spectroscopic, while the $4d, 4f, 5s, 5p,$ and $5d$ orbitals are correlation functions and are chosen to improve the energies of the ionic thresholds and the ground state of Cl^+ . The parameters of the various radial orbitals are presented in Table II. In the CIV3 calculation, we retained all configurations within the $n=5$ complex that had weights greater than 0.001. The wave functions are represented by a J -dependent CI expansion of the form [41]

$$\Psi_i(JM_J) = \sum_{j=1}^K b_{ij} \phi_j(\alpha_j L_j S_j JM_J), \quad (5)$$

where each of the K single-configuration functions ϕ_j is constructed from one-electron functions and α_j defines the coupling of the orbital L_j and spin S_j angular momenta to give the total angular momentum J . The mixing coefficients b_{ij} are obtained by diagonalizing the Breit-Pauli Hamiltonian, here composed of the nonrelativistic term plus the one-body mass correction, the Darwin term, and spin-orbit, spin-other-orbit, and spin-spin operators, with respect to the basis ϕ_j . The inclusion of mass correction, Darwin, and spin-spin terms shifts the energy of a configuration as a whole, while the spin-orbit and spin-other-orbit terms cause the fine-structure splitting. Our results for the Cl^+ target energies are given in Table III. The present results compare suitably with an

TABLE II. Cl^+ radial orbitals generated using the program CIV3. The $1s$ and $2s$ orbitals are those of Clementi and Roetti [39].

Orbital	Power of r	Exponent	Coefficient
$2p$	2	7.28476	0.70274
	2	12.72004	0.06182
	3	2.47884	0.03055
$3s$	3	6.61369	-0.00472
	3	5.97974	0.28597
	1	16.69807	-0.01598
	1	16.53109	0.11667
	2	4.39075	-0.78912
	2	12.26833	0.05024
	3	4.14479	0.70482
$3p$	3	2.30861	0.80404
	3	11.85510	-0.05906
	2	2.01665	2.52459
	2	9.11977	0.12243
	3	3.60382	-1.00120
	3	2.71824	-1.00016
	3	2.03637	-1.59911
$3d$	3	2.8375752	0.2720268
	3	1.2014151	0.8279294
$4s$	1	12.53922	0.04733
	2	6.38589	-0.13826
	2	0.71332	-1.26651
$4p$	3	2.34017	0.75500
	2	6.80218	0.08557
	3	2.30900	-0.32558
	4	0.91874	1.03629
$4d$	3	5.78397	-0.01010
	4	0.51295	1.25755
$4f$	4	0.92788	-0.47250
	4	0.50173	1.00000
	5	13.61950	0.02481
$5s$	2	5.43655	-0.11268
	2	0.47084	3.26529
	3	0.84030	-3.09910
	3	2.83392	0.14870
$5p$	2	6.82329	0.05013
	3	2.29310	-0.19781
	4	0.52269	-1.52140
$5d$	4	0.87440	1.11799
	3	19.64933	0.02782
	4	6.47903	2.32148
	4	5.04994	-1.63194

experimental determination of the energies of the $2p$ -hole states of Cl^+ [15]; and, for the lower states, the NIST values [42]. The ordering of energy levels is the same in both theory and experiment (with one possible exception), and the splitting of the levels is generally quite close, much closer than the absolute energies. It must be noted, however, that the present calculation aims primarily at an accurate spectral shape for the cross section, not absolute energies.

The fundamental reason that the 1S , 3P , and 1D $2p^{-1}$ states are higher than the 3S , 1P , and 3D states can be discerned from the expression for the Hartree-Fock (HF) energy. There is a large *monopole* exchange term $G^0(2p,3p)$ in the nonrelativistic HF energy of each of the LS states arising

TABLE III. LSJ target-state excitation energies (in a.u.) relative to the ground state of Cl^+ , calculated using the Breit-Pauli R -matrix code with optical potential along with experimental results [15,42].

Configuration	Term	J	Calculated	Experiment
$3s^23p^4$	$^3P^e$	2	0.00000	0.00000
$3s^23p^4$	$^3P^e$	1	0.003981	0.00317
$3s^23p^4$	$^3P^e$	0	0.00571	0.00454
$3s^23p^4$	$^1D^e$	2	1.84142	
$3s^23p^4$	$^1S^e$	0	4.18750	
$3s3p^5$	$^3P^o$	2	11.58987	
$3s3p^5$	$^3P^o$	1	11.69053	
$3s3p^5$	$^3P^o$	0	11.74316	
$3s^23p^3(^4S^o)4s$	$^3S^o$	1	14.55502	
$2p^53s^23p^5$	$(^1P^e)$	1	7.07962	7.16179
$2p^53s^23p^5$	$(^3D^e)$	3	7.08912	7.17377
$2p^53s^23p^5$	$(^3D^e)$	2	7.11567	
$2p^53s^23p^5$	$(^3D^e)$	1	7.13275	
$2p^53s^23p^5$	$(^3S^e)$	1	7.15469	7.22085
$2p^53s^23p^5$	$(^3P^e)$	2	7.17376	7.22916
$2p^53s^23p^5$	$(^3P^e)$	0	7.200125	7.24775
$2p^53s^23p^5$	$(^3P^e)$	1	7.20846	7.26609
$2p^53s^23p^5$	$(^1D^e)$	2	7.24651	7.29769
$2p^53s^23p^5$	$(^1S^e)$	0	7.32005	7.35645

from the $2p^{-1}$ configuration of Cl^+ . The coefficient of this term is -5 for all three of the lower-energy states and -3 for all three of the higher-energy states, so that, all other things being equal, one group of states is lower in energy by $2G^0$. Further differences accrue owing to the F^2 and G^2 terms in the HF energy, relativistic effects which split the 3P and 3D each into three states, and configuration-interaction effects on each of the states. But even with all of the other interactions, it is the HF G^0 term that determines that one group of $2p^{-1}$ states is lower in energy and the other group higher.

For the collision problem, the initial and final states are represented by the same type of Breit-Pauli R -matrix expansion. For Cl^+ , eight LS target symmetries ($^3P^e$, $^1D^e$, $^1S^e$, $^3P^o$, $^1P^o$, $^1P^e$, $^3D^e$, and $^3S^e$) were used, giving a total of 19 J levels, which include the crucial ten lowest $2p^53s^23p^5$ levels. This leads to a total of 484 configurations for Cl^+ with single electron promotions out of the $2p^63s^23p^4$, $2p^63s3p^5$, $2p^63p^6$, and $2p^53s^23p^5$ configurations. All $(N+1)$ -electron configurations consistent with double promotions out of the $2p^63s^23p^5$ configuration were used for the description of the various bound, resonant, and continuum states of Cl.

The specific processes of interest are inner-shell photoexcitation of the Cl ground state,

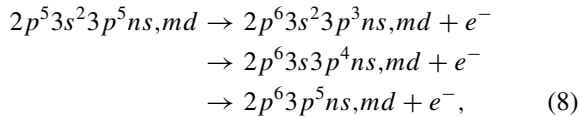
$$h\nu + 2p^63s^23p^5 \rightarrow 2p^53s^23p^5ns,md, \quad (6)$$

followed by two competing decay routes. First, there is *participator* Auger decay

$$2p^53s^23p^5ns,md \rightarrow 2p^63s^23p^4 + e^- \\ \rightarrow 2p^63s3p^5 + e^-, \quad (7)$$

where the valence electrons ns,md take part in the autoionization process; the decay rate therefore scales as $1/n^3$ ($1/m^3$). There is also the more important (yet less amenable

to close-coupling studies) *spectator* Auger decay



where the valence electrons ns, md do not take part in the autoionization process, giving instead a decay rate that is independent of n . Spectator Auger decay is therefore the dominant decay route as $n \rightarrow \infty$. A constant spectator width also leads to a smearing of higher- n resonances and a smooth transition from the below-threshold to above-threshold photoabsorption cross section.

In order to account for spectator Auger decay to the infinite number of continua in Eq. (8), the R matrix is modified by using an Auger optical potential [36], wherein the $2p^{-1}3p^{-1}$ Cl^+ energies are analytically continued into the complex plane via

$$E \rightarrow E - i\Gamma/2, \quad (9)$$

where Γ is the spectator Auger decay width and is computed in lowest-order perturbation theory using the program AUTOSTRUCTURE [43].

V. RESULTS AND DISCUSSION

Photofragmentation of the Cl_2 molecule at the L and K edges was reported in detail previously [30]. In the molecular system, the total charge is shared between the fragment ions, and ion charges from Cl^+ up to Cl^{3+} were observed at the L edge, and up to Cl^{5+} at the K edge. In the case of atomic chlorine, ionization at the L edge produces atomic ions with charge up to Cl^{3+} , seen in Fig. 4, and K -edge ionization leads to the production of ion charge up to Cl^{7+} , shown in Fig. 5. The ionization of atomic chlorine can be compared to the core-equivalent $Z + 1$ argon atom for which ion charges up to Ar^{4+} were observed at the L edge [44] and up to Ar^{7+} at the K edge [45]. When a $2p$ electron is ejected, the only possible

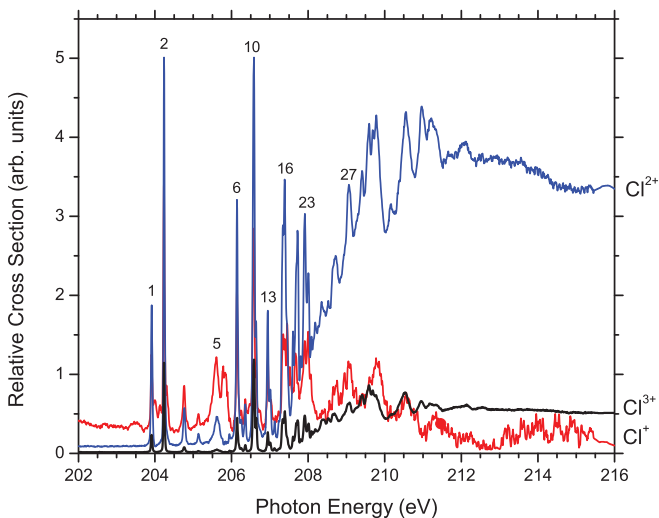


FIG. 4. (Color online) Relative partial cross sections for Cl^+ , Cl^{2+} , and Cl^{3+} resulting from photoexcitation of atomic Cl near the $L_{2,3}$ edges. The numbers located above spectral lines correspond to the index values N in Table I.

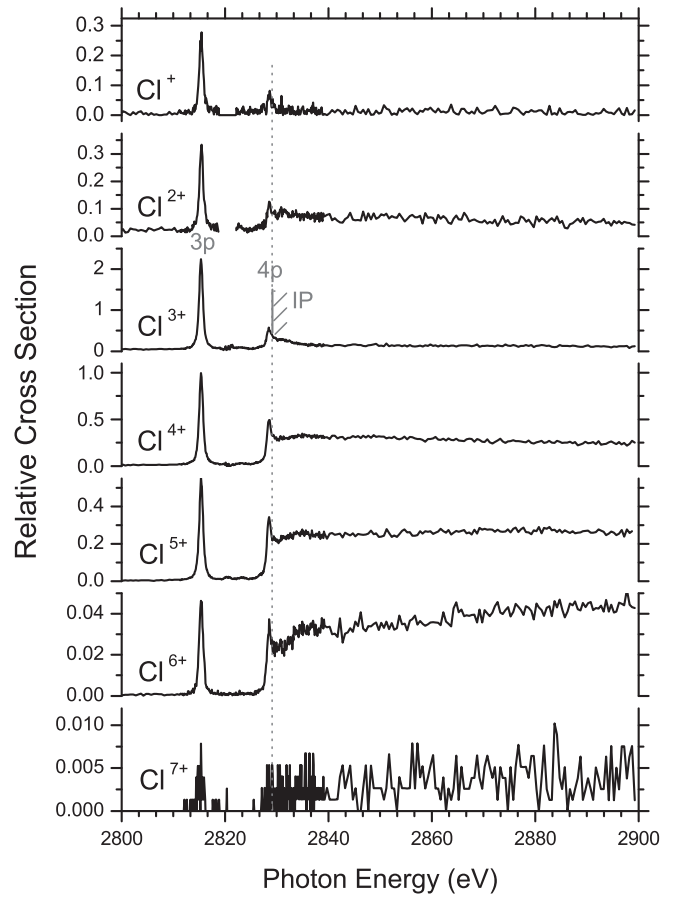


FIG. 5. Relative partial cross sections for Cl^n , $n = 1$ to 7 , resulting from photoexcitation of atomic Cl near the chlorine K edge. Due to high molecular chlorine contamination, the region near 2820 is not shown for Cl^+ and Cl^{2+} . The $3p$ and $4p$ transitions are located at 2815.4(1) and 2828.6(1). All errors are standard deviations and include the calibration to the $\text{Cl}(1s)^{-1} \rightarrow 11a_1$ transition in CF_3Cl at 2823.5 eV [31], which has an estimated 0.1 eV systematic error in photon energy.

pathway to produce singly charged ions is through LM radiative decay; similarly, when a K -shell electron is ejected, only KM radiative decay produces singly charged ions. In the case of argon, radiative decay is expected to account for 11% of the decay at the K edge and less than 1% at the L edge [46], and the yields are quite similar for Cl. The main decay channel to produce singly charged ions below the K threshold and doubly charged ions above the K threshold is KL x-ray emission followed by Auger LMM electron emission [46–48]. Recently, Ar $1s$ photoionization and subsequent Auger decay have been investigated in detail both experimentally by electron-ion coincidence measurements, and theoretically [49,50]. Decay pathways and lifetimes of the intermediate states involving both radiative and nonradiative processes for Ar^+ to Ar^{5+} have been reported. Below the L edge, singly charged ions are produced mainly through direct LMM Auger decay. No further decay occurs. The production of ions with charge higher than 2 is due to a primary Auger decay, KLL at the K edge [46,51,52]. The same processes and relative efficiencies are expected to be involved in the production of multiply charged ions in atomic chlorine. Thus, getting back to Fig. 4, Cl^{2+} is produced

Then, after applying angular-momentum algebra, the matrix element for the transition becomes

$$\sum_{S_1, L_1} (p^4 L_1 S_1 | \} p^5 L_c S_c) (2p^5 ({}^2P) \{ 3p^4 ({}^{2S_1+1}L_1) 3p ({}^2P) \} ({}^{2S_c+1}L_c) | V | 2p^6 ({}^1S) 3p^3 \epsilon p),$$

where the $(p^4 L_1 S_1 | \} p^5 L_c S_c)$ are the coefficients of fractional parentage and, importantly, are nonzero only if $S_1 + L_1 = \text{even}$, for this case of equivalent $3p^{-1}$ electrons. Then, applying further angular-momentum algebra, the transition matrix element becomes

$$\sum_{S_1, L_1, S_2, L_2} (p^4 L_1 S_1 | \} p^5 L_c S_c) (2p^5 ({}^2P) \{ 3p^4 ({}^{2S_1+1}L_1) 3p ({}^2P) \} ({}^{2S_c+1}L_c) | [2p^5 ({}^2P) 3p ({}^{2S_2+1}L_2)] 3p^4 ({}^{2S_1+1}L_1) ({}^{2S_c+1}L_c) \rangle \times ([2p^5 ({}^2P) 3p ({}^{2S_2+1}L_2)] 3p^4 ({}^{2S_1+1}L_1) ({}^{2S_c+1}L_c) | V | 2p^6 ({}^1S) 3p^3 \epsilon p)$$

involving additional angular-momentum recoupling coefficients on the second line. Now, as indicated above, the perturbation which engenders the Auger decay can be expanded in multipoles. If only the monopole ($\lambda = 0$) term, which is just $1/r_>$ and has no angular dependence, is considered, then it is clear that the initial and final states in the matrix must couple to exactly the same multiplet *for each coordinate* or the matrix element vanishes. In particular, for this case, the $2p^5 ({}^2P) 3p ({}^{2S_2+1}L_2)$ and $2p^6 ({}^1S)$ couplings must be the same, so that $S_2 = L_2 = 0$. This means that $S_1 = S_c, L_1 = L_c$ and, since it was shown above that $S_1 + L_1$ is even, then $S_c + L_c$ must be even for the monopole term to give a nonzero matrix element for the spectator Auger process, i.e., the monopole term contributes to the spectator Auger process only for $2p$ excitations leaving the 3P , 1S and 1D cores. The importance of this is that an excitation leaving the ion in the other core states cannot undergo the spectator Auger process via a monopole transition. The matrix element is decreased by a factor of 3 owing to the $1/(2\lambda + 1)$ in the expansion, which means that the width is lowered by an order of magnitude due to geometric effects alone. Over and above angular-momentum geometric effects, there are also dynamical effects due to the $r_<^\lambda / r_>^{\lambda+1}$ radial matrix element for $\lambda > 0$. This occurs because the region contributing materially to the radial transition matrix element in (r_1, r_2) space is reduced significantly with increasing λ , thereby reducing the radial transition matrix element integral. These differences, owing to the details of the angular-momentum coupling, are what cause three of the core states to exhibit much wider resonances than the other three. Our calculated results for the Cl^+ inner-shell vacancy widths are given in Table IV, where it is evident that two groups of widths are exhibited, and these groups differ by more than an order of magnitude. Note, however, that these are just the widths due to the spectator Auger process and not the total widths of the states.

But this is not the entire story, for there is a second reason why the resonances attached to the upper three $2p^5 3s^2 3p^5 ({}^{2S_c+1}L_c)$ ionic core states of Cl^+ are broader. Using an analysis similar to the discussion for the spectator-Augur transitions, one can show that the $2p \rightarrow ns, nd$ resonances corresponding to the higher-energy $2p^{-1}$ cores can autoionize to the lower $2p^{-1}$ cores of the same orbital angular momentum L_c , predominantly via a monopole exchange (spin-flip) transition, e.g., $2p^5 3s^2 3p^5 ({}^1S) 3d \rightarrow 2p^5 3s^2 3p^5 ({}^3S) \epsilon d$. But this monopole transition is forbidden between cores of different

L_c , which is why energetically allowed transitions between 3D and 1P cores are narrow. In any case, the existence of this monopole term in the rates between cores of the same L_c causes the resonances attached to the upper three core states (1S , 3D , and 1P) to be broader than those attached to the lower three (3S , 1D , and 3P); the lower resonance series do not have a lower-lying monopole transition continuum to which they can decay. Note that the broadness of these spin-flip transitions for the $2p^{-1}$ Auger transitions was pointed out previously [13].

As mentioned, the broad resonances are associated with the higher thresholds and are concentrated in the higher-energy region of Fig. 6. However, the lowest one or two resonances in a series converging to one of the higher thresholds might well be at much lower energy. This is seen in Table I, where the major resonances whose positions can be determined experimentally are shown, although, owing to the number and density of resonances, it is not entirely clear that the resonances derived from the experimental spectrum are each, in fact, single resonances, as opposed to two (or more) overlapping resonances. Note that this was also the conclusion of the earlier theoretical study (see Table 4 of Ref. [13]). In any case, in this table, the resonance labeled $N = 5$ at 205.618 eV is the only very wide one listed. It must be a $2p \rightarrow 4s$ resonance associated with the lowest even $S_c + L_c$ “wide-resonance” core state, the 3P_2 . This is in agreement with the results of the earlier theoretical study [13]. In connection with this earlier calculation, there are several resonances identified as being connected to odd $S_c + L_c$ core states that are found to be wide,

TABLE IV. Auger decay widths of the $2p^5 3s^2 3p^5 ({}^{2S_c+1}L_c)$ Cl^+ ionic states, computed using AUTOSTRUCTURE and neglecting fine-structure effects.

$S_c + L_c = \text{odd}$		Γ (meV)
	Term	
$2p^5 3s^2 3p^5$	(1P)	7.2
$2p^5 3s^2 3p^5$	(3D)	5.2
$2p^5 3s^2 3p^5$	(3S)	2.0
$S_c + L_c = \text{even}$		Γ (meV)
	Term	
$2p^5 3s^2 3p^5$	(3P)	173.9
$2p^5 3s^2 3p^5$	(1D)	163.4
$2p^5 3s^2 3p^5$	(1S)	147.8

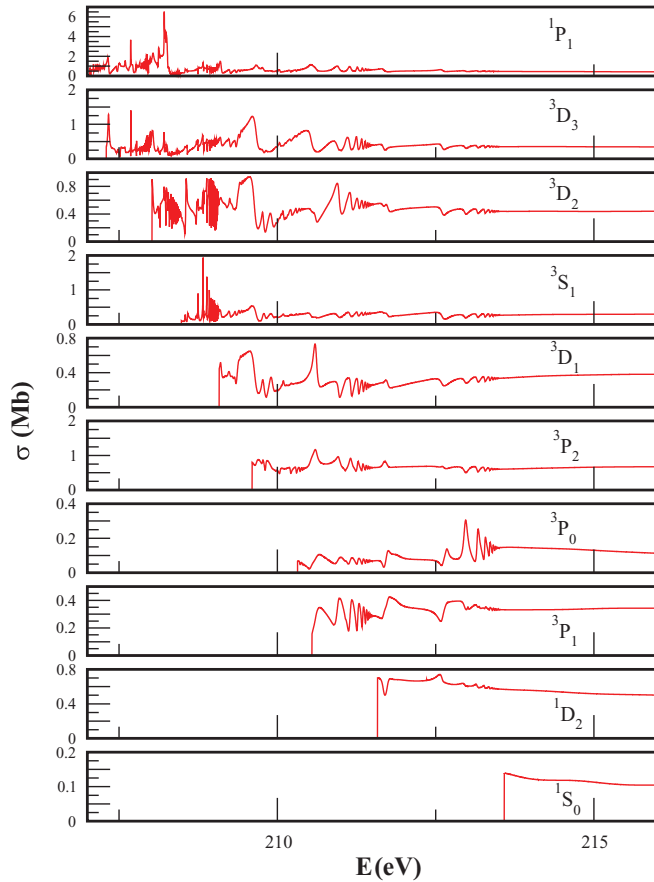


FIG. 7. (Color online) Theoretical photoionization cross sections (unconvoluted) of Cl in the $J = 3/2$ ground state for production of each of the ten $2p^{-1}$ states of Cl^+ . Note the difference in the scales of the various channels.

in contradiction to the present analysis. We believe that either these transitions are strongly mixed with resonances connected to even $S_c + L_c$ core states, or they are simply misidentified.

It is difficult to obtain a detailed picture from the *total* photoionization cross section owing to the plethora of resonances. To ameliorate this difficulty somewhat, the partial theoretical cross sections for leaving the Cl^+ ion in the ten possible $2p^{-1}$ states are shown in Fig. 7 for transitions from the initial $2^2P_{3/2}$ state of the Cl atom. Although these partial cross sections are considerably simpler than the total cross section, they are still quite complicated. The energy position and width of each resonance are properties of the resonance, i.e., they are the same in all photoionization channels, but the shapes of the resonances are very channel dependent as is evident from Fig. 7. The strength of each resonance also can differ quite a bit from channel to channel owing to the variation of decay rates to the various channels, again evident in Fig. 7. That there are overlapping resonance series is not really possible to discern from the total cross section, but examples can be seen in the partials. For example, in the 210 eV region of the 3D_2 cross section, a series of narrow resonances leading up to one threshold can be seen on the back of the lowest member of a very broad resonance series. A similar situation occurs just below 212 eV in the 1P_1 cross section, but this cannot be seen clearly owing to the scale of Fig. 7. It is important to note that the sum of these $2p^{-1}$

channel cross sections does not add up to the total cross section; the total cross section is the sum of these channel cross sections *plus* the sum of the cross sections of the channels leading to the $2p^63s^23p^4$, $2p^63s3p^5$, and $2p^63s^23p^34s$ states of the Cl^+ ion.

Using these partial cross sections, we have performed some analyses of the resonance series. As a general rule, in the absence of near-degeneracy of resonances converging to different thresholds (of which there are many), all of the $2p \rightarrow ns$ resonances that we can pick out exhibit quantum defects in the range of 1.80 to 1.90 for the higher resonances in each series; similarly, for the $2p \rightarrow nd$ resonances, the quantum defects for the higher members of the various series are 0.2 to 0.3. For the resonances of lower principal quantum number, $4s$, $5s$, and $6s$, along with $3d$ and $4d$, the quantum defects tend to get progressively larger with decreasing n . This phenomenon, the variability of the quantum defects for the lowest members of a resonance series, is not peculiar to the present case, nor is it associated with overlapping series of resonances, but it is a general characteristic of Rydberg resonance series [53]. However, using the range of quantum defects noted, resonances (or resonance series) can be separated into ns and nd series. For example, using the quantum defects inferred, we find that the broad series of resonances in the region of 213 eV are the $2p \rightarrow nd$ series leading up to the highest $2p^{-1}$ threshold, 1S_0 . These resonances are indicated by the experimental results, but not seen very clearly. The calculation shows them to be broad and very asymmetric in the *total* cross section. However, in the 3P_0 partial cross section (Fig. 7) these resonances are quite symmetric owing to a very low background cross section, and their energies can, thus, be picked out easily. Specifically, above the 1D_2 threshold (which lies just below 212 eV), are found the $5d$, $6d$, $7d$, and $8d$ members of the series with quantum defects of 0.28, 0.26, 0.23, and 0.19, respectively. Clearly the $3d$ and $4d$ members of this series lie below the 1D_2 threshold and their shapes are obliterated by the other resonances in this energy region. Note that characterizing a resonance by its quantum defect with respect to a particular threshold carries with it implicitly the designation of the resonance, so that is much more utilitarian than simply listing the resonance energy.

There is also a series of relatively broad resonances leading up to the 1D_2 threshold that are easy to pick out in the 3P_1 channel. Resonances from $5d$ to $10d$ are identified with quantum defects of 0.27 and 0.22 for the first two, and 0.20 for the rest of the series. The fact that the higher quantum defects are essentially constant means that we can predict the positions of all of the higher members of this resonance series using simple quantum defect ideas. In addition, the broad resonances leading up to the 3P_1 threshold, around 210 eV, are $2p \rightarrow ns$ resonances leading up to that threshold; these resonances appear to have been designated as nd resonances in Ref. [13], but the quantum defects of the present calculation indicate that they are misidentified in the earlier work. Although both of these resonance series are indicated experimentally, as seen in Fig. 6, they are not well defined enough to fit with a Fano profile to extract the detailed position and width; thus, they are not included in Table I. It is only with the comparison of theory and experiment that these resonances are identified. In any case, looking at the 3D_2 partial cross section, the $7s$ and

$8s$ members are identified with quantum defects of 1.86 and 1.82, respectively, which is strong evidence that they cannot be nd resonances.

In the energy region below these two series, a region that is dense with resonances, it is quite difficult to compare experiment and theory in great detail. Table I shows the 16 experimental resonances that can be picked out with some accuracy out of the hundreds that are part of the spectrum; most of these resonances have been dealt with adequately in the earlier theoretical work [13], so they will not be discussed further here. However, the partial cross sections, which make it easier to pick out resonance series, do clearly show that the resonances leading up to the higher-energy thresholds are much wider than the lower ones, in accordance with the earlier discussion. In other words, the detailed calculations demonstrated exactly what the general considerations predicted.

VI. FINAL REMARKS

Experimental photoionization cross sections for atomic chlorine in the vicinity of the $2p$ and the $1s$ thresholds have been measured, and Breit-Pauli R -matrix calculations have been performed in the region of the $2p$ excitations. We believe that the experimental results are the most accurate to date on the inner-shell photoionization of Cl, and the theoretical results are the most accurate essentially *ab initio* theoretical cross sections to date. It was shown that, owing to angular-momentum geometry, the resonances associated with the higher $2p^{-1}$ thresholds (1S , 3D , and 1P) should be much wider (decay much faster) than the resonances associated with the lower thresholds. This prediction is borne out both by the detailed theoretical calculations and by the experimental data. Note that, although the conclusions concerning resonance widths are applicable only to the present case (including the other halogen atoms), the method of analysis, i.e., looking at the possible multipolarities of Auger transitions allowed by angular-momentum considerations, should be generally applicable to inner-shell photoionization.

Agreement between theory and experiment was seen to be reasonable, thereby indicating that most of the important physics was included in the present calculations. That the theoretical results had to be shifted by 2.29 eV to reasonably match the experimental cross section is an endemic problem with R -matrix calculations, particularly for inner-shell calculations where the orbitals are optimized for the inner-shell

hole states, rather than for outer-shell excitations. Also, the experimental results were relative, and were normalized to theory at one energy; if a different energy were chosen to normalize, the comparison with theory could have been rather different. For example, if the experimental cross section is lowered by about 15%, then there is quite excellent agreement in the resonance range around 210 eV. Furthermore, in addition to getting the ordering of the $2p^{-1}$ thresholds right, it is of importance to get the relative energies of the thresholds correctly as well, since the whole pattern of resonance structure is crucially dependent upon these relative energies; accurate experimental determination of these thresholds via photoelectron spectroscopy or by some other means is, thus, a high-priority item.

It was also shown that there is a huge number of resonance series embedded in these data, and in many energy regions the overlapping of the various series precluded the possibility of easy characterization, particularly from the experimental data. Looking at the various $2p^{-1}$ partial cross sections, more detail was revealed. In that connection, in order to make a truly detailed comparison of experiment and theory, in addition to the experimental photoionization spectroscopy results presented herein, both photoelectron spectroscopy to determine the partial cross sections of the individual $2p^{-1}$ photoabsorption channels, along with Auger electron spectroscopy to pin down the branching ratios from a given excitation to the various final channels, would be very helpful to untangle all of the many facets of this extremely complicated spectrum.

ACKNOWLEDGMENTS

The authors thank the staff of the ALS for their excellent support. Support from the National Science Foundation under NSF Grant No. PHY-09-70125 is gratefully acknowledged. G.Ö. wishes to acknowledge a postdoctoral grant from The Swedish Foundation for International Cooperation in Research and Higher Education (STINT). T.W.G. was supported in part by NASA (Grant No. NNX11AF32G). This work was performed at the Advanced Light Source, which is supported by DOE (Grant No. DE-AC03-76SF00098). S.T.M., Z.F., and A.Z.M. were supported by DOE, Office of Basic Energy Sciences, Atomic Molecular and Optical Sciences Program, Grants No. DE-FG02-03ER15428 for S.T.M. and No. DE-FG02-97ER14743 for Z.F. and A.Z.M. The calculations were performed at the NERSC computational facility.

-
- [1] J. A. R. Samson, Y. Shefer, and G. C. Angel, *Phys. Rev. Lett.* **56**, 2020 (1986).
 - [2] J. A. R. Samson and G. C. Angel, *Phys. Rev. A* **42**, 1307 (1990).
 - [3] E. de Beer, C. A. de Lange, and N. P. C. Westwood, *Phys. Rev. A* **46**, 5653 (1992).
 - [4] M. O. Krause, C. D. Caldwell, S. B. Whitfield, C. A. de Lange, and P. van der Meulen, *Phys. Rev. A* **47**, 3015 (1993).
 - [5] S. J. Schaphorst, S. B. Whitfield, H. P. Saha, C. D. Caldwell, and Y. Azuma, *Phys. Rev. A* **47**, 3007 (1993).
 - [6] J. Jiménez-Mier, S. J. Schaphorst, C. D. Caldwell, and M. O. Krause, *Phys. Rev. A* **56**, 3659 (1997).
 - [7] C. D. Caldwell, M. O. Krause, R. D. Cowan, A. Menzel, S. B. Whitfield, S. Hallman, S. P. Frigo, and M. C. Severson, *Phys. Rev. A* **59**, R926 (1999).
 - [8] P. van der Meulen, M. O. Krause, C. D. Caldwell, S. B. Whitfield, and C. A. de Lange, *Phys. Rev. A* **46**, 2468 (1992).
 - [9] S. B. Whitfield, S. Hallman, M. O. Krause, C. D. Caldwell, and R. D. Cowan, *Phys. Rev. A* **60**, R1747 (1999).

- [10] M. M. Sant'Anna, A. S. Schlachter, G. Öhrwall, W. C. Stolte, D. W. Lindle, and B. M. McLaughlin, *Phys. Rev. Lett.* **107**, 033001 (2011).
- [11] S. N. Nahar and S. T. Manson, *Phys. Rev. A* **40**, 5017 (1989).
- [12] B. Ruscic and J. Berkowitz, *Phys. Rev. A* **40**, 6716 (1989).
- [13] M. Martins, *J. Phys. B* **34**, 1321 (2001).
- [14] Z.-w. Wang and K. T. Lu, *Phys. Rev. A* **31**, 1515 (1985).
- [15] N. J. Wilson, K. L. Bell, and A. Hibbert, *J. Phys. B* **33**, L341 (2000).
- [16] K. Schofield, *J. Quant. Spectrosc. Radiat. Transfer* **17**, 13 (1977).
- [17] V. Vaida, S. Solomon, E. C. Richard, E. Rühl, and A. Jefferson, *Nature (London)* **342**, 405 (1989).
- [18] R. Atkinson, D. L. Baulch, R. A. Cox, J. N. Crowley, R. F. Hampson, R. G. Hynes, M. E. Jenkin, M. J. Rossi, and J. Troe, *Atmos. Chem. Phys.* **7**, 981 (2007).
- [19] M. Martins, K. Godehusen, T. Richter, P. Wernet, and P. Zimmermann, *J. Phys. B* **39**, R79 (2006).
- [20] S. A. Sheinerman, *J. Phys. B* **36**, 4435 (2003).
- [21] D. P. Almeida, A. C. F. Santos, M. G. P. Homem, A. N. de Brito, and G. G. B. de Souza, *J. Electron Spectrosc. Relat. Phenom.* **155**, 109 (2007).
- [22] N. M. Kabachnik, S. Fritzsche, A. N. Grum-Grzhimailo, M. Meyer, and K. Ueda, *Phys. Rep.* **451**, 155 (2007).
- [23] A. G. Kochur, A. I. Dudenko, I. D. Petrov, and V. F. Demekhin, *J. Electron Spectrosc. Relat. Phenom.* **156–158**, 78 (2007).
- [24] B. Crasemann, *Can. J. Phys.* **176**, 251 (1988).
- [25] Y. Lu, W. C. Stolte, and J. A. R. Samson, *Phys. Rev. A* **58**, 2828 (1998).
- [26] Y. Hikosaka, P. Lablanquie, F. Penent, P. Selles, T. Kaneyasu, E. Shigemasa, J. H. D. Eland, and K. Ito, *Phys. Rev. A* **80**, 031404(R) (2009).
- [27] W. C. Stolte, Y. Lu, J. A. R. Samson, O. Hemmers, D. L. Hansen, S. B. Whitfield, H. Wang, P. Glans, and D. W. Lindle, *J. Phys. B* **30**, 4489 (1997).
- [28] J. A. R. Samson and P. N. Pareek, *Phys. Rev. A* **31**, 1470 (1985).
- [29] D. A. Shaw, G. C. King, and F. H. Read, *J. Phys. B* **13**, L723 (1980).
- [30] W. C. Stolte, R. Guillemin, R. Demchenko, G. Öhrwall, S.-W. Yu, J. A. Young, M. Taupin, O. Hemmers, M. N. Piancastelli, and D. W. Lindle, *J. Phys. B* **43**, 155202 (2010).
- [31] R. C. C. Perera, P. L. Cowan, D. W. Lindle, R. E. LaVilla, T. Jach, and R. D. Deslattes, *Phys. Rev. A* **43**, 3609 (1991).
- [32] M. Simon, L. Journal, R. Guillemin, W. C. Stolte, I. Minkov, F. Gel'mukhanov, P. Salek, H. Ågren, S. Carniato, R. Taïeb, A. C. Hudson, and D. W. Lindle, *Phys. Rev. A* **73**, 020706(R) (2006).
- [33] W. C. Stolte, R. Guillemin, S.-W. Yu, and D. W. Lindle, *J. Phys. B* **41**, 145102 (2008).
- [34] T. Ressler, computer code WINXAS (Hamburg, Germany, 2009).
- [35] K. A. Berrington, W. B. Eissner, and P. H. Norrington, *Comput. Phys. Commun.* **92**, 290 (1995).
- [36] T. W. Gorczyca and F. Robicheaux, *Phys. Rev. A* **60**, 1216 (1999).
- [37] T. W. Gorczyca, *Phys. Rev. A* **61**, 024702 (2000).
- [38] T. W. Gorczyca and B. M. McLaughlin, *J. Phys. B* **33**, L859 (2000).
- [39] E. Clementi and C. Roetti, *At. Data Nucl. Data Tables* **14**, 177 (1974).
- [40] A. Hibbert, *Comput. Phys. Commun.* **9**, 141 (1975).
- [41] R. Glass and A. Hibbert, *Comput. Phys. Commun.* **16**, 19 (1978).
- [42] A. Kramida, Yu. Ralchenko, and J. Reader, *NIST Atomic Spectra Database (version 5.1)*, NIST ASD Team (National Institute of Standards and Technology, Gaithersburg, MD., 2013), <http://physics.nist.gov/asd>.
- [43] N. R. Badnell, *J. Phys. B* **19**, 3827 (1986).
- [44] J. A. R. Samson, Z. X. He, W. C. Stolte, and J. N. Cutler, *J. Electron Spectrosc. Relat. Phenom.* **78**, 19 (1996).
- [45] K. Ueda, E. Shigemasa, Y. Sato, A. Yagishita, M. Ukai, H. Maezawa, T. Hayaishi, and T. Sasaki, *J. Phys. B* **24**, 605 (1991).
- [46] A. G. Kochur, V. L. Sukhorukov, A. I. Dudenko, and Ph. V. Demekin, *J. Phys. B* **28**, 387 (1995).
- [47] U. Alkemper, J. Doppelfeld, and F. von Busch, *Phys. Rev. A* **56**, 2741 (1997), and references therein.
- [48] P. Lablanquie, L. Andric, J. Palaudoux, U. Becker, M. Braune, J. Viehhaus, J. H. D. Eland, and F. Penent, *J. Electron Spectrosc. Relat. Phenom.* **156–158**, 51 (2007).
- [49] R. Guillemin, S. Sheinerman, C. Bomme, L. Journal, T. Marin, T. Marchenko, R. K. Kushawaha, N. Trcera, M. N. Piancastelli, and M. Simon, *Phys. Rev. Lett.* **109**, 013001 (2012).
- [50] R. Guillemin, C. Bomme, T. Marin, L. Journal, T. Marchenko, R. K. Kushawaha, N. Trcera, M. N. Piancastelli, and M. Simon, *Phys. Rev. A* **84**, 063425 (2011).
- [51] J. C. Levin, C. Biedermann, N. Keller, L. Liljeby, C.-S. O, R. T. Short, I. A. Sellin, and D. W. Lindle, *Phys. Rev. Lett.* **65**, 988 (1990).
- [52] G. B. Armen, J. C. Levin, and I. A. Sellin, *Phys. Rev. A* **53**, 772 (1996).
- [53] U. Fano and J. W. Cooper, *Rev. Mod. Phys.* **40**, 441 (1968).